

Hydrothermal synthesized magnetically separable mesostructured $H_2Ti_3O_7/\gamma-Fe_2O_3$ nanocomposite for organic dye removal via adsorption and its regeneration/reuse through synergistic non-radiation driven H_2O_2 activation

Harsha Narayani, Manu Jose, K. Sriram & Satyajit Shukla

Environmental Science and Pollution Research


ISSN 0944-1344
Volume 25
Number 21

Environ Sci Pollut Res (2018)
25:20304-20319
DOI 10.1007/s11356-017-8381-2



Your article is protected by copyright and all rights are held exclusively by Springer-Verlag Berlin Heidelberg. This e-offprint is for personal use only and shall not be self-archived in electronic repositories. If you wish to self-archive your article, please use the accepted manuscript version for posting on your own website. You may further deposit the accepted manuscript version in any repository, provided it is only made publicly available 12 months after official publication or later and provided acknowledgement is given to the original source of publication and a link is inserted to the published article on Springer's website. The link must be accompanied by the following text: "The final publication is available at link.springer.com".

Hydrothermal synthesized magnetically separable mesostructured $\text{H}_2\text{Ti}_3\text{O}_7/\gamma\text{-Fe}_2\text{O}_3$ nanocomposite for organic dye removal via adsorption and its regeneration/reuse through synergistic non-radiation driven H_2O_2 activation

Harsha Narayani^{1,2} · Manu Jose^{1,2} · K. Sriram¹ · Satyajit Shukla^{1,2} 

Received: 14 November 2016 / Accepted: 3 January 2017 / Published online: 14 February 2017
© Springer-Verlag Berlin Heidelberg 2017

Abstract Hydrogen titanate ($\text{H}_2\text{Ti}_3\text{O}_7$) nanotubes/nanosheets (HTN) are emerging class of adsorbent material which possess unique property of activating hydrogen peroxide (H_2O_2) to generate the reactive oxygen species (ROS), such as superoxide radical ions ($\text{O}_2^{\cdot-}$) and hydroxyl radicals ($\cdot\text{OH}$), effective in the decomposition of surface-adsorbed dye. However, HTN are non-magnetic which create hurdle in their effective separation from the treated aqueous solution. To overcome this issue, magnetic nanocomposites (HTNF) composed of HTN and maghemite ($\gamma\text{-Fe}_2\text{O}_3$) nanoparticles have been processed by subjecting the core-shell magnetic photocatalyst consisting of $\gamma\text{-Fe}_2\text{O}_3$ /silica (SiO_2)/titania (TiO_2), having varying amounts of TiO_2 in the shell to the hydrothermal conditions. HTNF-5 magnetic nanocomposite consisting of 31 wt% $\text{H}_2\text{Ti}_3\text{O}_7$, typically having nanotube morphology with the highest specific surface area ($133 \text{ m}^2 \text{ g}^{-1}$) and pore-volume ($0.22 \text{ cm}^3 \text{ g}^{-1}$), exhibits the highest capacity (74 mg g^{-1}) for the adsorption of cationic methylene blue (MB) dye from an aqueous solution involving the electrostatic attraction

mechanism and pseudo-second-order kinetics. Very fast magnetic separation followed by regeneration of HTNF-5 magnetic nanocomposite has been demonstrated via non-radiation driven H_2O_2 activation. It has been ascertained for the first time that the underlying mechanism of dye decomposition involves the synergy effect between the constituents of HTNF magnetic nanocomposite.

Keywords Adsorption · Dye · Reactive oxygen species · Isotherm · Kinetics · Magnetic separation · Recycling

Abbreviations

AP	3-Aminophthalate
BET	Brunauer–Emmett–Teller
BJH	Barrett–Joyner–Halenda
DKR	Dubinin–Kaganer–Radushkevich
DTA	Differential thermal analysis
EDTA	Ethylenediaminetetraacetic acid
EDX	Energy dispersive X-ray
EPR	Electron paramagnetic resonance
FTIR	Fourier transform infrared
HRTEM	High-resolution transmission electron microscope
HTN	Hydrogen titanate nanotubes/nanosheets
HTNF	Hydrogen titanate nanotubes/nanosheets-maghemite
JCPDS	Joint Committee on Powder Diffraction Standards
MB	Methylene blue
PL	Photoluminescence
PPMS	Physical property measurement system
ROS	Reactive oxygen species
SAED	Selected area electron diffraction
SS	Stainless steel
SSA	Specific surface area
STA	Simultaneous thermal analyzer

Responsible editor: Suresh Pillai

Electronic supplementary material The online version of this article (doi:10.1007/s11356-017-8381-2) contains supplementary material, which is available to authorized users.

✉ Satyajit Shukla
satyajit_shukla@niist.res.in

¹ Functional Materials Section (FMS), Materials Science and Technology Division (MSTD), Council of Scientific and Industrial Research (CSIR), CSIR-National Institute for Interdisciplinary Science and Technology (NIIST), Industrial Estate P.O., Pappanamcode, Thiruvananthapuram, Kerala 695019, India

² Academy of Scientific and Innovative Research (AcSIR), CSIR-NIIST Campus, Thiruvananthapuram, Kerala 695019, India

TA	Terephthalic acid
TEM	Transmission electron microscope
TG	Thermal gravimetry
TSF	Maghemite/silica/titania
UV	Ultraviolet
VSM	Vibrating sample magnetometer
XPS	X-ray photoelectron spectroscope
XRD	X-ray diffraction

Introduction

In the photocatalytic degradation of organic pollutants, the magnetic photocatalyst based on the sol-gel-derived core-shell maghemite/silica/titania ($\gamma\text{-Fe}_2\text{O}_3/\text{SiO}_2/\text{TiO}_2$) (TSF) nanocomposite has been the most commonly reported system in which the photocatalytic and magnetic properties are provided by TiO_2 and $\gamma\text{-Fe}_2\text{O}_3$ (Liu 2012). The interlayer of SiO_2 avoids the direct electrical contact between the core ($\gamma\text{-Fe}_2\text{O}_3$) and the shell (TiO_2) which enhances the photocatalytic activity. It also avoids the transformation of magnetic $\gamma\text{-Fe}_2\text{O}_3$ to non-magnetic hematite ($\alpha\text{-Fe}_2\text{O}_3$) during the high temperature calcination treatment. Moreover, it prevents the photo-dissolution of Fe^{2+} ions into the surrounding aqueous solution during photocatalysis process without affecting the photocatalytic activity (Beydoun et al. 2002). However, to overcome some of the major limitations of magnetic photocatalyst which include the need for radiation exposure, reduced efficiency, and delayed degradation of dyes in highly concentrated solutions, the development of adsorbent-based magnetic nanocomposites has been initiated (Sivashankar et al. 2014). It has been demonstrated that the hydrothermal treatment of TiO_2 -coated SiO_2 -based fly ash particles results in the stabilization of nanosheets of hydrogen titanate which exhibits enhanced adsorption properties compared to that of nanotube morphology (Hareesh et al. 2012). However, such a hydrothermal transformation to titanate-based magnetic adsorbents using the $\gamma\text{-Fe}_2\text{O}_3/\text{SiO}_2/\text{TiO}_2$ magnetic photocatalyst as a precursor has never been demonstrated. Hence, it is interesting to investigate the processing of titanate-based magnetic adsorbents via hydrothermal treatment of $\gamma\text{-Fe}_2\text{O}_3/\text{SiO}_2/\text{TiO}_2$ magnetic photocatalyst which is not reported in the literature.

Thazhe et al. (2010) first derived the titanate nanotube-based magnetic nanocomposite via hydrothermal treatment of sol-gel derived core-shell cobalt ferrite (CoFe_2O_4)/ $\text{SiO}_2/\text{TiO}_2$ which was subsequently modified by Li et al. (2011). Zhou et al. (2015a) and Papa et al. (2011) demonstrated that the hydrothermal treatment of magnetic nanoparticles dispersed along with TiO_2 in an alkali solution with the formation of magnetic titanates which is also the modification

of former method. In spite of these earlier efforts in the conversion of core-shell magnetic photocatalyst to magnetic dye-adsorbent catalyst via hydrothermal, the precise morphological evolution during the hydrothermal treatment of $\gamma\text{-Fe}_2\text{O}_3/\text{SiO}_2/\text{TiO}_2$ magnetic photocatalyst as a function of amount of TiO_2 in the shell and its effect on the adsorption characteristics of newly developed products have not been studied in the literature. Hence, in this investigation, we synthesize $\gamma\text{-Fe}_2\text{O}_3/\text{SiO}_2/\text{TiO}_2$ magnetic photocatalyst via sol-gel method containing different amount of TiO_2 in the shell and study its effect on the morphological evolution of titanate-based magnetic products of hydrothermal treatment and their adsorption characteristics.

Recently, we demonstrated that the formation of hydrogen titanate ($\text{H}_2\text{Ti}_3\text{O}_7$)/ $\gamma\text{-Fe}_2\text{O}_3$ magnetic nanocomposites via a strong ion-exchange bond formation at the interface between magnetic nanoparticles and titanate nanotubes (Harsha et al. 2015). In the earlier study, the weight fraction of $\gamma\text{-Fe}_2\text{O}_3$ in the magnetic nanocomposite was varied in the narrower and lower range of 5–25 wt%. In the present investigation, however, using the combination of sol-gel and hydrothermal methods, the magnetic nanocomposites having the weight fraction of $\gamma\text{-Fe}_2\text{O}_3$ in the higher range of 61–92 wt% could be synthesized. It is to be noted that the different synthesis techniques, such as the ion-exchange and sol-gel/hydrothermal, when combined together, can produce the magnetic nanocomposites covering the entire range of weight fraction of $\gamma\text{-Fe}_2\text{O}_3$. This is not possible to obtain by any of the unique technique either due to the processing issues or due to the formation of free $\gamma\text{-Fe}_2\text{O}_3$ nanoparticles which are not attached to the nanotubes (Harsha et al. 2015).

Relative to the costlier carbon-based (Gracia-Espino et al. 2012) and low-cost adsorbents (Gupta and Suhas 2009), the titanate-based magnetic adsorbents investigated in this work concurrently offer several advantages in the dye removal application such as the operation of ion-exchange and electrostatic attraction mechanisms for adsorption (Lee et al. 2008; Bavykin et al. 2010), easy tailoring of surface chemistry to increase the adsorption capacity (Lee et al. 2012), easy solid-liquid separation using an external magnetic field by attaching them to the magnetic nanoparticles (Harsha et al. 2015), and fast regeneration of catalyst via hydrogen peroxide (H_2O_2) activation process conducted in the dark (Babu et al. 2014; Shukla et al. 2014; Shukla and Oturan 2015). In this investigation, we demonstrate the magnetic separation of hydrogen titanate nanotubes/nanosheets-maghemite (HTNF) magnetic nanocomposite from an aqueous dye solution followed by its regeneration via non-radiation driven H_2O_2 activation. The underlying physical mechanism of dye decomposition, involving the generation and attack of reactive oxygen species (ROS), such as the superoxide radical ions ($\text{O}_2^{\cdot-}$) and hydroxyl radicals ($\cdot\text{OH}$), is revealed for the first time using the radical-trapping experiments.

Materials and methods

Materials

Titanium(IV)-isopropoxide ($\text{Ti}(\text{OC}_3\text{H}_7)_4$, 97%), tetraethyl orthosilicate (TEOS, 98%), nanocrystalline $\gamma\text{-Fe}_2\text{O}_3$ (<50 nm, 98%) magnetic powder, and terephthalic acid (TA, 98%) were purchased from Sigma-Aldrich Chemicals, Bengaluru, India; hydrochloric acid (HCl, 35 wt%) from Ranbaxy Fine-Chemicals, India; ammonium hydroxide (NH_4OH , 25 wt%) from Qualigens Fine Chemicals, India; ethanol (99.9% AR), 2-propanol (99.5%, ACS reagent), sodium hydroxide (NaOH, Assay 97%), MB (96%), and H_2O_2 (30 wt%) from S.D. Fine-Chem Ltd., Mumbai, India; and Luminol (5-Amino-2,3-dihydrophthalazine-1,4-dione) from Merck Specialties Pvt. Ltd., India. All listed chemicals were used as-received without any further purification and/or modification.

Sol-gel synthesis of core-shell $\gamma\text{-Fe}_2\text{O}_3/\text{SiO}_2/\text{TiO}_2$ magnetic photocatalyst

The core-shell $\gamma\text{-Fe}_2\text{O}_3/\text{SiO}_2/\text{TiO}_2$ nanocomposites of different TiO_2 weight fractions were prepared by the combination of modified Stober and sol-gel methods similar to that reported in our previous investigation (Narayani et al. 2013a). Briefly, a continuous uniform coating of SiO_2 over $\gamma\text{-Fe}_2\text{O}_3$ nanoparticles was obtained via controlled hydrolysis of TEOS using NH_4OH solution in the ethanol medium. The product obtained was washed with distilled water, then with ethanol, and finally dried at room temperature. TiO_2 coating over $\gamma\text{-Fe}_2\text{O}_3/\text{SiO}_2$ nanocomposite was performed via hydrolysis of $\text{Ti}(\text{OC}_3\text{H}_7)_4$ in 2-propanol in several number of cycles (1, 3, 5, and 7 cycles) in order to get TiO_2 -coated $\gamma\text{-Fe}_2\text{O}_3/\text{SiO}_2$ with increasing amount of TiO_2 content which are denoted as TSF-1, TSF-3, TSF-5, and TSF-7, respectively. Theoretical calculations show that the weight fraction of anatase- TiO_2 in TSF-1, TSF-3, TSF-5, and TSF-7 samples varies as 6, 17, 26, and 33 wt%, respectively (note: for the precise determination of amount of TiO_2 deposited on the surface of $\gamma\text{-Fe}_2\text{O}_3/\text{SiO}_2$, the final weight of $\gamma\text{-Fe}_2\text{O}_3/\text{SiO}_2/\text{TiO}_2$ magnetic nanocomposite obtained is considered in the calculations instead of initial amount of $\text{Ti}(\text{OC}_3\text{H}_7)_4$ used).

Hydrothermal synthesis of $\text{H}_2\text{Ti}_3\text{O}_7/\gamma\text{-Fe}_2\text{O}_3$ magnetic nanocomposite

Two grams of TSF sample was suspended in a highly alkaline NaOH solution (10 M) taken in a Teflon beaker (84 vol%) which was placed in a stainless steel (SS 316) vessel of 200 ml capacity. The hydrothermal reaction was carried out in an autoclave (Amar Equipments Pvt. Ltd., Mumbai, India) at 120 °C for 30 h. The autoclave was allowed to cool naturally

to room temperature and the product was collected by decanting the top solution. Then, the latter was first washed using 100 ml of 1 M HCl solution for 1 h followed by that using 100 ml of pure distilled water for 1 h for multiple times till pH (Hanna HI 2210 Bench Top, Sigma-Aldrich, India) of filtrate became almost neutral. The washed product was then separated from the solution using a centrifuge (Hettich EBA 20, Sigma-Aldrich, India) and dried in an oven at 80 °C (termed as the final hydrothermal product). Depending on the precursor used, the final hydrothermal product was denoted as HTNF-1, HTNF-3, HTNF-5, and HTNF-7, respectively. Theoretical calculations show that the fraction of HTN in HTNF-1, HTNF-3, HTNF-5, and HTNF-7 magnetic nanocomposites varies as 8, 21, 31, and 39 wt%, respectively (note: since the SiO_2 coating gets dissolved during the hydrothermal process, the amount of Si species readsorbed on the surface of magnetic nanocomposites is not considered in the calculation of weight fraction of constituents of HTNF).

Characterization

The morphology of different samples was examined using the transmission electron microscope (TEM) (Tecnai G², FEI, The Netherlands) operated at 300 kV, and their nanocrystalline nature was confirmed from the selected-area electron diffraction (SAED) patterns. The chemical constituents of different samples were identified using the energy dispersive X-ray (EDX) analysis. The crystal structure was determined using the X-ray diffraction (XRD, PW1710 Phillips) technique by utilizing $\text{Cu K}\alpha$ X-radiation ($\lambda_{\text{Cu}} = 1.5406 \text{ \AA}$). The XRD patterns were obtained at room temperature over 2θ values within the range of 10°–80°. The specific surface area of the samples, average pore size, and its distribution were measured via Brunauer–Emmett–Teller (BET) surface area measurement technique (Micrometrics Gemini 2375 Surface Area Analyzer) by using nitrogen (N_2) adsorption–desorption multi-point method. The samples were degassed in the flowing N_2 atmosphere at 200 °C before the measurements. Thermal gravimetric and differential thermal analysis (TG/DTA) studies were carried out (PerkinElmer, Model STA 6000 simultaneous TG-DTA, The Netherlands) in an ambient atmosphere with the heating rate of 10 °C min^{-1} under N_2 purge within the temperature range of 50–1000 °C. A blank run was conducted, before the experiment, using alumina for the baseline correction. The surface chemistry of different samples was analyzed using the Fourier transform infrared (FTIR, IRPrestige-21 Shimadzu, Japan) spectroscope within the frequency range of 4000–400 cm^{-1} using the powders dispersed in the potassium bromide (KBr) pellets. The magnetic properties were analyzed using a vibrating sample magnetometer (VSM) attached to a physical property measurement system (PPMS, Quantum Design, Dynacool, USA). The zeta-potential measurements were performed using the

electrophoretic light scattering in the pH range from 2 to 10 using a Zetasizer Nano Series-Zen 3600 (Malvern Instruments, UK).

Dye adsorption characteristics of $\text{H}_2\text{Ti}_3\text{O}_7/\gamma\text{-Fe}_2\text{O}_3$ magnetic nanocomposite

The time-dependent adsorption of MB on the surface of HTNF samples was carried out via the procedure already described in our previous report (Harsha et al. 2015). The measurements were conducted in 125 ml aqueous solutions of MB having the initial concentration within the range of 7.5–250 μM at the initial solution-pH of 10 adjusted using NH_4OH solution, with the adsorbent concentration of 0.4 g l^{-1} (note: the dye adsorption measurements as reported earlier for pure-HTN suggest that, within the initial solution-pH range of 2.5–11, the maximum adsorption capacity is obtained at the initial solution-pH of 10; Narayani et al. 2013b). The aliquots (4 ml) collected at the definite time intervals were analyzed, after the catalyst separation, by recording the absorption spectra obtained using the UV–visible spectrophotometer (UV-2401 PC, Shimadzu). After the equilibrium adsorption, the magnetic HTNF samples were separated by providing a small bar magnet outside the vial. The normalized concentration of surface-adsorbed MB dye was derived using the following equation

$$\% \text{MB}_{\text{adsorbed}} = \left(\frac{C_o - C_t}{C_o} \right)_{\text{MB}} \times 100 \quad (1)$$

This is equivalent to the form

$$\% \text{MB}_{\text{adsorbed}} = \left(\frac{A_o - A_t}{A_o} \right)_{\text{MB}} \times 100 \quad (2)$$

where C_o and C_t (mg l^{-1}) represent the unadsorbed and residual MB concentrations at the initial and after the contact time t with the corresponding absorbance of A_o and A_t . The intensity of maximum absorbance peak of MB dye solution, located at 656 nm, was taken as a measure of residual concentration of MB dye.

Regeneration and reuse of HTNF magnetic nanocomposite by decomposition of surface-adsorbed MB dye

The recycling was achieved via magnetic separation of MB adsorbed HTNF sample and its regeneration via catalytic decomposition of previously adsorbed dye molecules through non-radiation driven H_2O_2 activation in an aqueous solution. The recycling was demonstrated using HTNF-5 magnetic nanocomposite (0.4 g l^{-1}) in 125 ml aqueous solution of MB dye having the initial concentration of 30 μM at the initial solution-pH of 10. After the first cycle of MB adsorption, a

bar magnet was placed outside the container to attract the magnetic nanocomposite on its walls and the treated solution was decanted. The bar magnet was removed, and fresh 10 ml distilled H_2O was poured into the container to collect the magnetic nanocomposite sticking on the walls of container. The aqueous suspension of magnetic nanocomposite was then dried in an oven at $80 \text{ }^\circ\text{C}$ overnight, and the dried sample was utilized for the second cycle of dye adsorption measurement conducted under the similar test conditions. Total six successive cycles of dye adsorption measurements were conducted without the use of any intermediate regeneration treatment. Later, the dye adsorption experiments were repeated with the involvement of regeneration treatment which was conducted after the end of each cycle of dye adsorption. In the latter, the dried HTNF-5 sample (0.4 g l^{-1}) with the MB dye adsorbed on its surface was dispersed in 100 ml of 15 wt% (4.5 M) H_2O_2 solution (obtained via dilution method) and stirred using an overhead stirrer (IKA, Eurostar Digital, Germany) for 3 h (note: the selection of 15 wt% (4.5 M) H_2O_2 solution is in accordance with Jose et al. (2014) who demonstrated that the higher the initial MB concentration, the higher the initial H_2O_2 concentration required to decompose MB dye completely in 1 h under the dark condition. In the present investigation, the use of 3 wt% (0.9 M) H_2O_2 solution could not regenerate HTNF-5 sample even after 3 h of contact time). The regenerated catalyst was separated from the aqueous solution using an external magnetic field provided by a small bar magnet; and after drying in an oven at $80 \text{ }^\circ\text{C}$ overnight, it was recycled for the next cycle of dye adsorption. Total six successive cycles of dye adsorption measurements were conducted with the use of intermediate regeneration treatment.

Detection of ROS ($\text{O}_2^{\cdot-}$ and $\cdot\text{OH}$)

Luminol was used as a chemiluminescent probe for the detection of generated $\text{O}_2^{\cdot-}$. Luminol (0.278 g l^{-1}) was dissolved in 125 ml of alkaline (0.4 g l^{-1} NaOH) H_2O_2 (15 wt% (4.5 M)) solution. After 1 h of overhead stirring, 0.4 g l^{-1} of HTNF-5 sample was added with the continued stirring. Aliquot (8 ml) was then collected after 10 min of contact time. The magnetic nanocomposite was separated from the sample suspension using a bar magnet, and the solution obtained was immediately subjected to PL emission spectral analysis (Cary Eclipse, Varian, The Netherlands). The luminol molecules react with the generated $\text{O}_2^{\cdot-}$ species and produce 3-aminophthalate (AP) which exhibits a characteristic broad PL peak normally located at 420 nm at an excitation wavelength of 350 nm, the intensity of which is taken as the measure of generated amount of $\text{O}_2^{\cdot-}$ species (Nosaka et al. 1997). In the present work, this emission peak was located within the wavelength range of 425–429 nm (note: H_2O_2 solution, in the absence of magnetic nanocomposite, also contains small amount of $\text{O}_2^{\cdot-}$ species. The intensity of PL peak obtained

from this blank solution is considered as a reference peak (background) and is subtracted from the PL intensity observed in the presence of a magnetic nanocomposite).

For the $\cdot\text{OH}$ detection, an alkaline solution of TA was used which upon excitation at 315 nm normally provides an emission peak at 425 nm due to the formation of 2-hydroxyterephthalic acid as a result of the reaction between TA and generated free $\cdot\text{OH}$. (Ishibashi et al. 2000). In the present work, this emission peak was located within the wavelength range of 437–445 nm. The experiments were similar to the previous case except that the concentration of NaOH and TA were changed to 0.08 and 0.058 g l⁻¹, respectively. Similar to the previous case, the background subtraction is conducted in this case as well using the blank solution. The O₂⁻ and $\cdot\text{OH}$ trapping experiments were also conducted using pure HTN (0.124 g l⁻¹) and pure $\gamma\text{-Fe}_2\text{O}_3$ (0.276 g l⁻¹) nanoparticles. For these typical experiments, the concentration of respective catalyst was determined from its weight fraction in the HTNF-5 sample. All other experimental parameters were similar to those as described above.

Results and discussion

Morphological, chemical, and structural evolution of hydrothermal processed H₂Ti₃O₇/ $\gamma\text{-Fe}_2\text{O}_3$ magnetic nanocomposite

The core-shell TSF magnetic nanocomposites having varying amount of TiO₂ are obtained via multiple sol-gel TiO₂-coating cycles. The morphologies of TSF magnetic nanocomposites as observed using TEM analysis have been already reported by Narayani et al. 2013a and also by others (Abramson et al. 2009; Yu et al. 2011; Wang et al. 2009). Typical morphologies of HTNF magnetic nanocomposites evolved, subsequent to hydrothermal treatment of TSF samples, as observed using TEM images obtained at lower and higher magnifications, are presented in Figs. 1 and 2. The corresponding EDX patterns are shown in Fig. S1 of Online Resource. It is noted that the core-shell TSF magnetic nanocomposite consists of three components $\gamma\text{-Fe}_2\text{O}_3$, SiO₂, and anatase-TiO₂. Among these components, $\gamma\text{-Fe}_2\text{O}_3$ is inactive under the hydrothermal conditions and remains intact in the final hydrothermal products. However, according to Hareesh et al. (2012) and Li et al. (2011), SiO₂ and TiO₂ layers undergo chemical reactions in highly alkaline hydrothermal conditions forming SiO₄⁴⁻ ions and nanosheets/nanotubes of hydrogen titanate, respectively, which remain dissolved or suspended in the surrounding aqueous solution. In Fig. 1a, the average size of $\gamma\text{-Fe}_2\text{O}_3$ nanoparticles is noted to be ~25 nm with no direct evidence of presence of H₂Ti₃O₇ phase. However, EDX pattern presented in Fig. S1a (see the Online Resource) does show the existence of tiny amount of Ti in this sample along

with the significant presence of Fe and Cu (note: Cu originates from the grid used for TEM analysis).

For HTNF-3 sample (Fig. 1b), $\gamma\text{-Fe}_2\text{O}_3$ nanoparticles are observed to be surrounded by the nanosheets of H₂Ti₃O₇ which are also clearly seen in Fig. 2a at higher magnification. The formation of nanotube morphology of H₂Ti₃O₇ is not evident in these images. On the contrary, for HTNF-5 sample (Fig. 1c), $\gamma\text{-Fe}_2\text{O}_3$ nanoparticles are observed to be surrounded by nanotubes of H₂Ti₃O₇, having the average length of 150 nm and average inner diameter of 4 nm, which are undoubtedly seen in Fig. 2b at higher magnification. In contrast to the previous samples, the formation of nanosheet morphology of H₂Ti₃O₇ is not noticeable in these images. However, for HTNF-7 sample (Fig. 1d), $\gamma\text{-Fe}_2\text{O}_3$ nanoparticles are observed to be surrounded by mixed nanosheets and nanotubes of H₂Ti₃O₇ which are also evident in Fig. 2c at higher magnification. Moreover, the layered structured H₂Ti₃O₇ nanosheets are observed to be formed in a relatively larger amount and exhibit a highly aggregated morphology (note: $\gamma\text{-Fe}_2\text{O}_3$ nanoparticles are intercalated in between and attached to the edges of nanosheets and occupy interaggregate pores. These factors have possibly reduced the contrast of nanoparticles in the TEM image; Fig. 1d). The corresponding EDX patterns (see Fig. S1a–c, respectively, of Online Resource) reveal a gradual increase in Ti content (2, 15, and 25 at.%) with the increasing number of sol-gel TiO₂-coating cycles. However, for the HTNF-7 sample, a decrease in Ti content (11 at.%) is observed which is attributed to the pickup of large amount of Si by this sample (see Fig. S1d of Online Resource). No free islands of H₂Ti₃O₇ nanotubes or nanosheets are observed in all TEM images presented in Figs. 1 and 2 suggesting the formation of a nanocomposite instead of mixture of former with $\gamma\text{-Fe}_2\text{O}_3$ nanoparticles. Moreover, the high-resolution TEM (HRTEM) image (Fig. 2d) shows the average interlayer spacing of 0.78 nm which is close to that of (200) plane of H₂Ti₃O₇ as reported by Wu et al. (2006).

The XRD patterns of as-received $\gamma\text{-Fe}_2\text{O}_3$ nanoparticles and HTNF samples are shown in Fig. 3a, while that of pure HTN is shown separately in Fig. 3b due to relatively lower intensity of diffraction peaks. It is noted that all of HTNF samples strongly exhibit the XRD pattern of $\gamma\text{-Fe}_2\text{O}_3$ nanoparticles according to JCPDS card no. 39-1346 (see the section-B (Figs. S2 and S3) in the Online Resource for further analysis using the XRD, FTIR, and HRTEM results for the justification of identified phase in the as-received magnetic nanoparticles). Small intensity XRD peaks of HTN ($2\theta = 24.5^\circ$ and 48.5°) are assigned to either pure H₂Ti₃O₇ or lepidocrocite-type titanate in accordance with Kitano et al. (2013). It is to be noted that the variation in the intensity of XRD peaks corresponding to H₂Ti₃O₇

Fig. 1 Low magnification TEM images of HTNF-1 (a), HTNF-3 (b), HTNF-5 (c), and HTNF-7 (d) samples. The lower-left corner insets show the corresponding SAED patterns

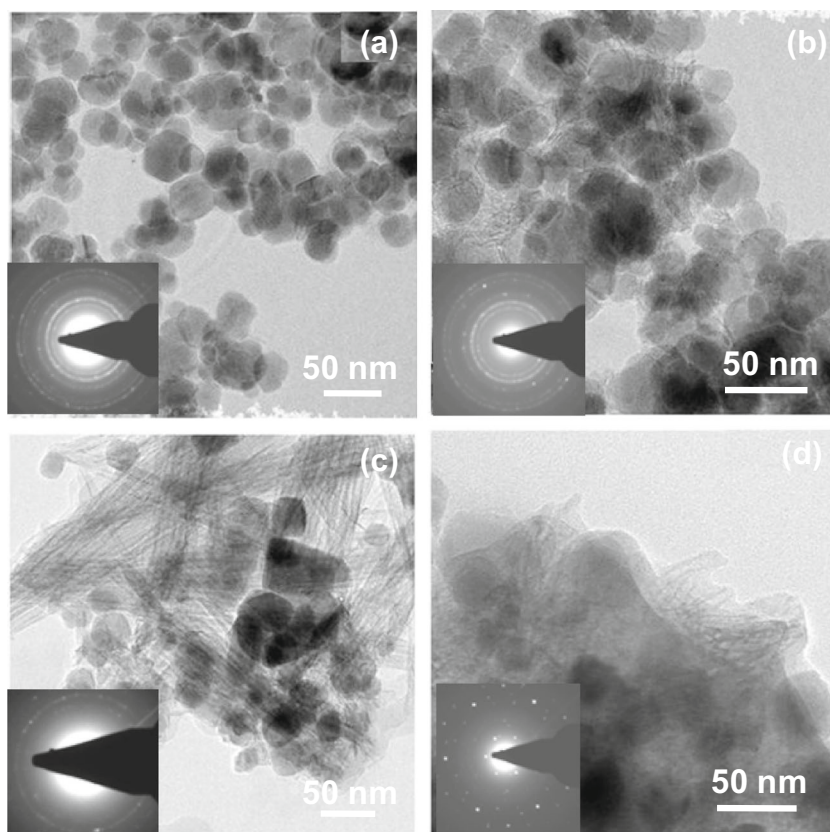
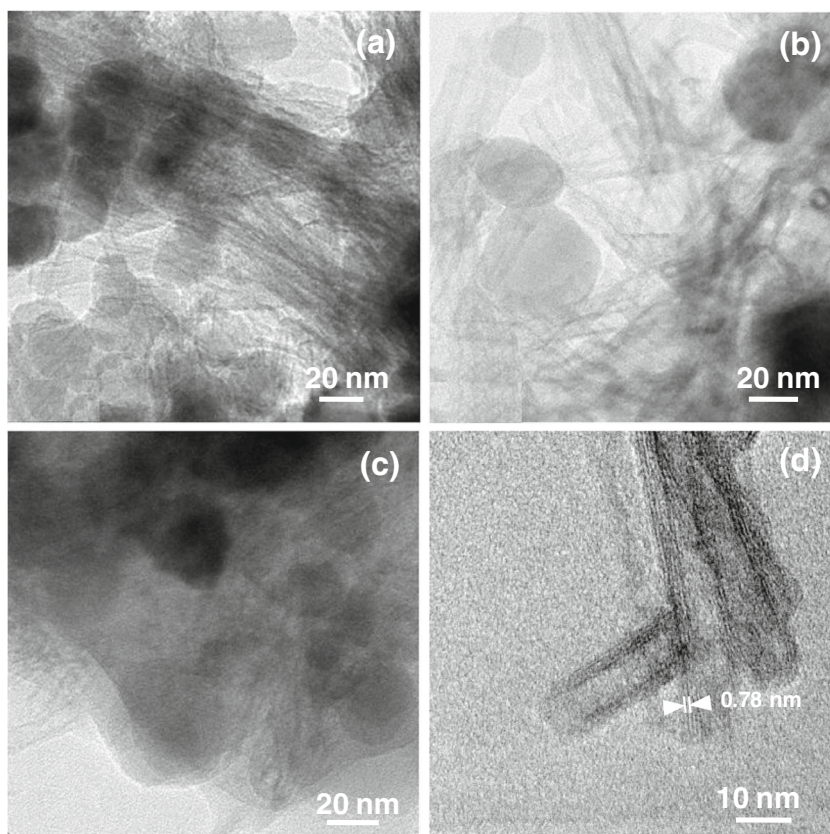


Fig. 2 High magnification TEM images of HTNF-3 (a), HTNF-5 (b), and HTNF-7 (c) samples. d HRTEM image of pure HTN showing the measurement of average spacing between the lattice fringes



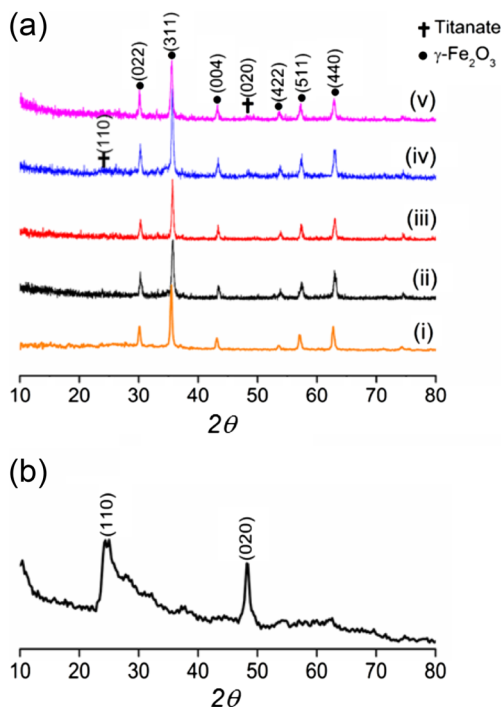


Fig. 3 XRD patterns of HTNF (a) and pure HTN (b) samples. In a, XRD patterns vary as pure $\gamma\text{-Fe}_2\text{O}_3$ (i), HTNF-1 (ii), HTNF-3 (iii), HTNF-5 (iv), and HTNF-7 (v) samples

(Fig. 3a) is not commensurate with the weight fraction of HTN in the HTNF samples which is due to very low crystallinity of HTN relative to that of $\gamma\text{-Fe}_2\text{O}_3$ nanoparticles. However, such correlation can be easily established from the EDX analysis presented in Fig. S1 (see the Online Resource) except for HTNF-7 sample for which the large amount of Si pickup is observed.

The N_2 adsorption–desorption isotherms of pure HTN and HTNF magnetic nanocomposites are shown in Fig. 4a (note: see the TG/DTA results presented in Fig. S4 and the related discussion in the Online Resource). The isotherms are recognized as type II, while the hysteresis loops correspond to type H3 which are the characteristics of slit-shaped mesopores. This is in agreement with the characteristics of HTNF magnetic nanocomposites processed via ion-exchange method as reported earlier by Harsha et al. (2015). The Barrett–Joyner–Halenda (BJH) pore-size distribution curves for the above samples are shown in Fig. 4b. It is observed that narrow and small intensity peaks in the pore-size distribution curve appear in between 2 and 6 nm regions which are ascribed to the inner diameter of HTN consistent with the TEM results. The continuous increase in the pore volume after 6 nm pore size is related to the aggregates of nanotubes having non-uniform pore volume in between them.

The BET specific surface area of 38, 81, 133, and $121 \text{ m}^2 \text{ g}^{-1}$ and the pore volume of 0.07, 0.15, 0.22, and $0.19 \text{ cm}^3 \text{ g}^{-1}$ are, respectively, observed for HTNF-1, HTNF-3, HTNF-5, and HTNF-7 samples. The values of these

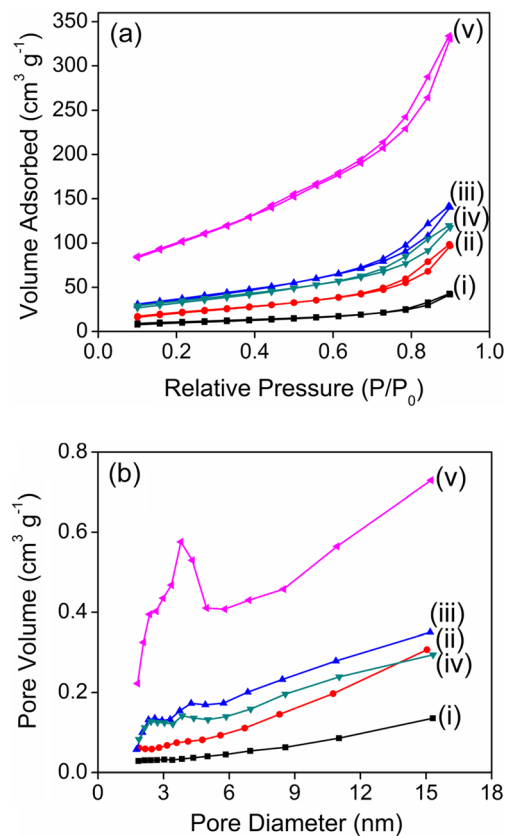


Fig. 4 N_2 adsorption–desorption isotherms (a) and BJH pore-size distribution curves (b) as obtained for HTNF-1 (i), HTNF-3 (ii), HTNF-5 (iii), HTNF-7 (iv), and pure HTN (v) samples

parameters for pure $\gamma\text{-Fe}_2\text{O}_3$ nanoparticles and pure HTN are noted to be 32 and $362 \text{ m}^2 \text{ g}^{-1}$ and 0.00045 and $0.53 \text{ cm}^3 \text{ g}^{-1}$, respectively. Both the specific surface area and pore volume of HTNF samples, thus, fall in between those of pure $\gamma\text{-Fe}_2\text{O}_3$ nanoparticles and pure HTN. It is noted that both the specific surface area and pore volume increase with the number of sol-gel TiO_2 -coating cycles, except for cycle-7 where a decrease in the values of these parameters is noted which is attributed to highly aggregated nature of relatively large number of layered structured $\text{H}_2\text{Ti}_3\text{O}_7$ nanosheets as obtained under this processing condition. Thus, the attachment of non-magnetic HTN to magnetic $\gamma\text{-Fe}_2\text{O}_3$ nanoparticles via hydrothermal reactions results in a net increase in the specific surface area (from 32 to $38\text{--}133 \text{ m}^2 \text{ g}^{-1}$) and pore volume (from 0.00045 to $0.07\text{--}0.22 \text{ cm}^3 \text{ g}^{-1}$) of HTNF magnetic nanocomposites which have been attributed to higher specific surface area and pore volume of pure HTN compared with those of $\gamma\text{-Fe}_2\text{O}_3$ nanoparticles. It strongly appears that the dominance of either attractive or repulsive forces in between the magnetic $\gamma\text{-Fe}_2\text{O}_3$ nanoparticles also contributes to the actual variation in the specific surface area and pore volume as a function of amount of $\gamma\text{-Fe}_2\text{O}_3$ nanoparticles varying within the range of 0–100 wt% (see Fig. S5 and related discussion in the Online Resource).

Mechanism of morphological evolution of hydrothermal processed HTNF magnetic nanocomposite

The mechanism of morphological evolution of HTNF samples along with the changes in their structural and chemical constituents as a function of number of sol-gel TiO₂-coating cycles, as confirmed via TEM, EDX, XRD, and BET analyses, is summarized in the model proposed in Fig. 5. As shown in the model, γ -Fe₂O₃ nanoparticles are coated with SiO₂ via modified Stober process followed by sol-gel coating of TiO₂

over γ -Fe₂O₃/SiO₂ nanocomposite particles. The amount of TiO₂ (that is, the average thickness of TiO₂ coating) is controlled by increasing the number of sol-gel TiO₂-coating cycles. Moreover, the average aggregate size of γ -Fe₂O₃/SiO₂ nanocomposite particles over which TiO₂ coating takes place is assumed to increase with the number of sol-gel TiO₂-coating cycles as per the model suggested earlier by Zhou et al. (2015a).

For the cycles 1 and 3, final hydrothermal products contain the nanosheets of H₂Ti₃O₇. It appears that the average TiO₂

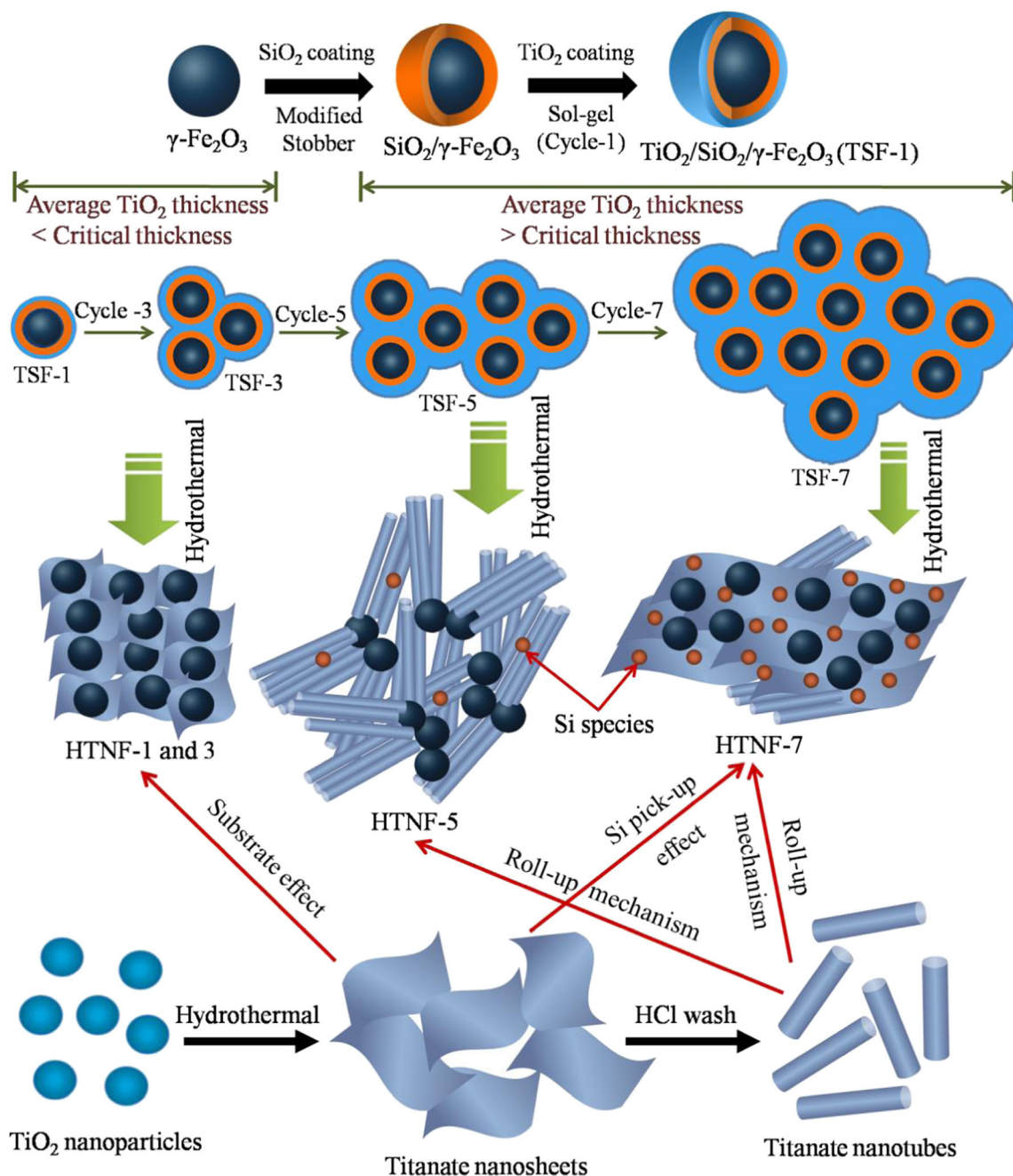


Fig. 5 Model describing the morphological evolution of HTNF magnetic nanocomposites hydrothermally processed using TSF samples synthesized with different of number of sol-gel TiO₂-coating cycles

thickness under these processing conditions is below the critical thickness required to avoid the substrate effect which is the result of a strong bond formation at the interface of γ -Fe₂O₃ nanoparticles and H₂Ti₃O₇ via ion-exchange reactions (Harsha et al. 2015) (note: this further supports the presence of a nanocomposite of γ -Fe₂O₃ nanoparticles and H₂Ti₃O₇ instead of their mixture in the final hydrothermal product). As suggested by Lu et al. (2011), the nanocrystalline particles of anatase-TiO₂ in a freestanding powder are converted to the nanotubes of H₂Ti₃O₇ via roll-up mechanism involving the sequential transformation of nanoparticles to nanosheets and then to nanotubes. It appears that when the thickness of sol-gel TiO₂ coating is below the critical thickness, the substrate effect does not allow the roll-up mechanism to go to completion resulting in the stabilization of intermediate nanosheet morphology. As per the TEM analysis (Fig. 1a, b) and the model presented in the Fig. 5, this is particularly observed for TSF-1 and TSF-3 samples. Since, the amount of Si pick up is minimum (see Fig. S1a, b of Online Resource), the effect of Si pickup on the stabilization of nanosheet morphology is ruled out for these two samples. For the TSF-5 sample, the average thickness of sol-gel TiO₂ coating is assumed to be larger than the critical thickness (Fig. 5). In this case, as a result of minimization of substrate effect and minimum Si pickup by this sample (see Fig. S1c of Online Resource), the nanocrystalline TiO₂ coating is effectively converted to nanotubes of H₂Ti₃O₇ via roll-up mechanism without any stabilization of intermediate nanosheet morphology. The gradual increase in the specific surface area and pore volume from HTNF-1 to HTNF-5 sample is attributed to the corresponding increase in the weight fraction of HTN in these samples.

For TSF-7 sample, the average sol-gel TiO₂ coating thickness is also assumed to be larger than the critical thickness (Fig. 5) required to avoid the substrate effect. Hence, similar to the previous case, the formation of only nanotube morphology is expected for this sample as well. In contrast to this, the formation of both nanosheets and nanotubes (predominantly nanosheets) is observed (Figs. 1d and 2c). The formation of mixed morphologies in the case of HTNF-7 sample is a result of large amount of Si pickup by this sample (see Fig. S1d of Online Resource), which is possibly due to the intercalation of SiO₄⁴⁻ ions within the layered structure of highly aggregated nanosheets of H₂Ti₃O₇. The stabilization of intermediate nanosheet morphology of H₂Ti₃O₇ by surface adsorption of Si species during the hydrothermal treatment has been reported earlier by Hareesh et al. (2012) (see the Scheme S1 and related discussion in the Online Resource for the Si pickup effect). There is also a strong possibility of contribution of non-uniform distribution of Si species which may allow the formation of nanotubes at the specific locations where the concentration of Si species is relatively lower allowing the nanosheets to roll up to form nanotubes. The decrease in the specific surface area and pore volume of this sample

compared with those of HTNF-5 sample is ascribed to the effect of strong aggregation tendency of nanosheets and their large fraction in the nanocomposite relative to that of nanotubes, which are superimposed on the magnetic effect (see Fig. S5 of Online Resource). Thus, the formation of either nanosheets, nanotubes, or mixed morphologies for hydrothermal processed HTNF magnetic nanocomposite as a function of increasing number of sol-gel TiO₂-coating cycles is primarily governed by the roll-up mechanism superimposed with substrate and Si pickup effects.

MB adsorption characteristics of HTNF magnetic nanocomposites

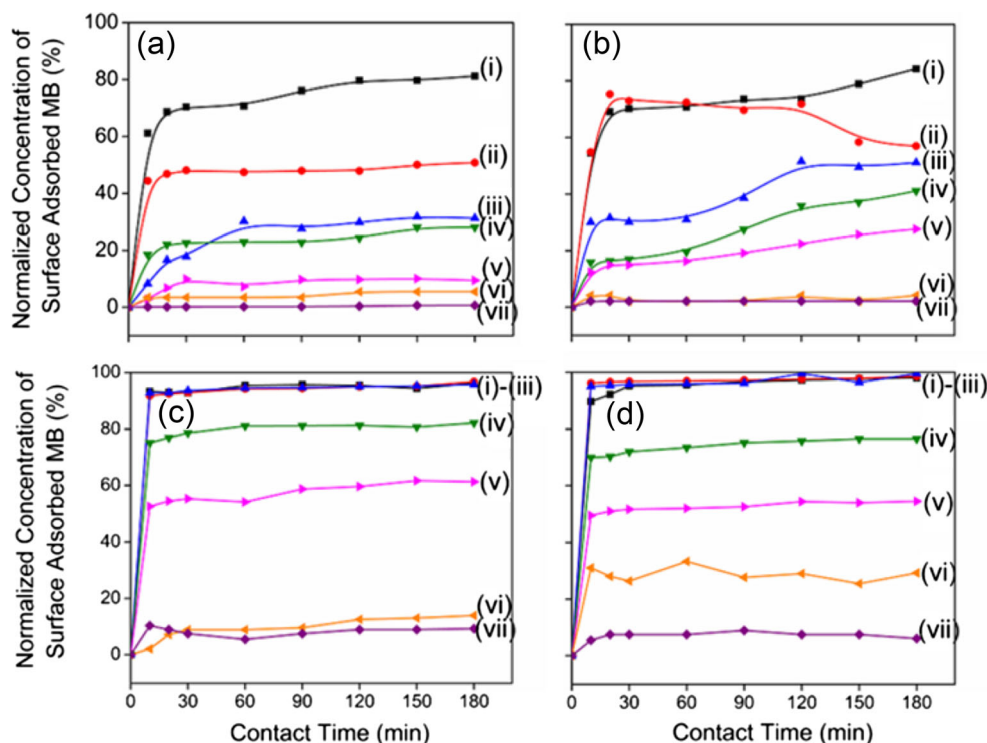
The adsorption performance of HTNF magnetic nanocomposites is studied by varying the initial MB concentration within the range of 7.5–250 μ M. The time-dependent variations in the normalized concentration of surface-adsorbed MB (derived using Eqs. 1 and 2) at the initial solution-pH of 10 are presented in Fig. 6 for different HTNF samples. The adsorption equilibrium is attained within the first 10 min of contact time which is attributed to the dominance of strong electrostatic interaction between the negatively charged surface of HTN and cationic MB molecules at the initial solution-pH of 10 as suggested earlier by Harsha et al. (2015) and Bavykin et al. (2010). The normalized equilibrium concentration of MB adsorbed on the surface of HTNF is decreased with increasing initial MB dye concentration.

The amount of MB adsorbed after the elapse of specific amount of time, t , can be expressed as the amount of dye molecules adsorbed (mg) per unit weight of HTNF sample (g), which is of the form (Jose et al. 2014; Harsha et al. 2015)

$$q_t = \frac{(C_o - C_t)V}{m_{HTN}} \quad (3)$$

where C_o and C_t (mg Γ^{-1}) represent dye concentrations at the initial ($t = 0$ min) and after the contact time of t (min), m_{HTN} (g) the mass of adsorbent, and V (l) the initial volume of solution. The variation in the calculated values of q_t as a function of contact time as obtained for different HTNF samples is shown in Fig. S6, while the equilibrium adsorption isotherm curves are presented in Fig. S7 of Online Resource. The variation in the values of equilibrium adsorption (q_e , for which $C_t = C_e$ where C_e is the residual dye concentration at equilibrium) as a function of initial MB concentration as obtained for various HTNF samples is plotted in Fig. 7. It is noted that q_e increases initially with the initial MB concentration, reaches the maximum value within the initial MB concentration range of 90–150 μ M, and then reduces with further increase in the initial MB concentration. The initial rise in q_e is attributed to greater driving force for the gradual consumption of more number of active surface sites available on the surface of HTNF samples. It is to be

Fig. 6 Variations in the normalized concentration of surface-adsorbed MB as a function of contact time as obtained for HTNF-1 (a), HTNF-3 (b), HTNF-5 (c), and HTNF-7 (d) samples. The initial MB dye concentration is varied as 7.5 (i), 30 (ii), 60 (iii), 90 (iv), 150 (v), 200 (vi), and 250 μM (vii)



noted that the cationic MB molecules are adsorbed due to the electrostatic interaction with the negatively charged surface of HTNF samples which is provided by the presence of chemisorbed OH^- ions and Bronsted acidic nature of titanate surface resulting from the dissociation of $\text{H}_2\text{Ti}_3\text{O}_7$ as per the following reaction as suggested earlier by Bavykin et al. (2010) and Bavykin et al. (2006).



At higher initial MB concentrations, greater interaction of cationic MB molecules with OH^- ions within the solution

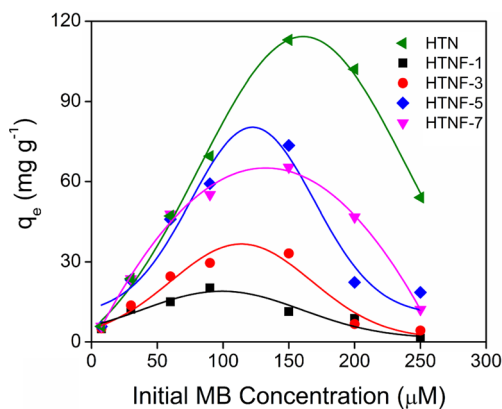


Fig. 7 Variation in q_e as a function of initial MB dye concentration as obtained for HTNF samples. The graph for pure HTN is shown for comparison as obtained from the data already presented elsewhere (Harsha et al. 2015)

possibly reduces the chemisorption of latter on the surface of HTNF samples. This is in consonance with Narayani et al. (2013b) who ascribed the decrease in q_e values at higher initial MB concentrations to decrease in the negative charge present on the surface of adsorbent as a result of reduction in the adsorption of OH^- ions on its surface due to their strong interaction with the cationic MB molecules within the solution.

The MB adsorption capacity (q_m) is estimated to be 20, 33, 74, and 65 mg g^{-1} for HTNF-1, HTNF-3, HTNF-5, and HTNF-7 samples, respectively. The MB adsorption capacity of $\gamma\text{-Fe}_2\text{O}_3$ nanoparticles and pure HTN is determined to be 13 and 113 mg g^{-1} (Harsha et al. 2015). Thus, the attachment non-magnetic HTN to magnetic $\gamma\text{-Fe}_2\text{O}_3$ nanoparticles via hydrothermal reactions results in a net increase in the MB adsorption capacity of HTNF magnetic nanocomposites from 13 to 20–74 mg g^{-1} which is attributed to higher MB adsorption capacity of pure HTN compared with that of $\gamma\text{-Fe}_2\text{O}_3$ nanoparticles. It strongly appears that the actual variation in the MB adsorption capacity of HTNF magnetic nanocomposites (see Fig. S8 and related discussion in the Online Resource) is well correlated with the similar variations in the specific surface area and pore volume as a function of amount of $\gamma\text{-Fe}_2\text{O}_3$ in accordance with the law of mixture superimposed with the magnetic effect (also see the Table S1 of Online Resource). Moreover, the zeta-potential measurements (see Fig. S9 of Online Resource) suggest that the points of zero charge for pure HTN, pure $\gamma\text{-Fe}_2\text{O}_3$ nanoparticles, and HTNF-5 samples are 4.7, 5.0, and 5.3, respectively. Typically, at the initial solution-pH of 8.0, they exhibit

the surface potential of -22.7 , -11.9 , and -30 mV, respectively.

It is noted that the MB adsorption capacity of HTNF samples lie in between that of pure $\gamma\text{-Fe}_2\text{O}_3$ nanoparticles and pure HTN. It is further noted that with increasing HTN content of magnetic nanocomposite samples, MB adsorption capacity is increased which is attributed to corresponding increase in the specific surface area and pore volume of samples. The dye adsorption capacity is, however, noted to decrease suddenly for HTNF-7 sample which is ascribed to its lower specific surface area and pore volume compared with those of HTNF-5 sample. The maximum MB adsorption capacity (74 mg g^{-1}) along with magnetic property is, thus, exhibited by HTNF-5 sample which appears to be the most optimum one (see the Table S2 of Online Resource for the comparison of maximum adsorption capacity of HTNF-5 sample with that of other magnetic adsorbents reported in the literature).

The time-dependent MB adsorption on the HTNF surface is analyzed using two different kinetics models—Lagergren pseudo-first-order and pseudo-second-order (Lagergren 1898; Ho and McKay 1998; Gunathilake et al. 2015) (see the section-L in the Online Resource). The linear plots (see Fig. S10 of Online Resource) with the regression correlation coefficient, $\langle r^2 \rangle$, approximately equal to one and the q_e values approximately equal to that of experimentally observed values, q_e (Exp) (see the Table S3 of Online Resource), suggest that the MB adsorption on the surface of HTNF magnetic nanocomposites follows the pseudo-second-order kinetics.

Adsorption isotherm study is very important to understand the nature of adsorbate–adsorbent interaction. The equilibrium adsorption of MB on the surface of HTNF samples is analyzed using three well-known adsorption isotherm models—Langmuir, Freundlich, and Dubinin–Kaganer–Radushkevich (DKR) (Gunathilake et al. 2015; Langmuir 1916; Tan et al. 2008; Freundlich 1906; Shen et al. 2010; Lakouraj et al. 2015) (see the section-O of Online Resource). The fitted curves for the equilibrium MB adsorption on the surface of HTNF-5 sample obtained using the above isotherm models are shown in Fig. 8 (also see the section-P of Online Resource). The calculated values of different parameters of these equilibrium isotherm models are listed in the Table S4 of Online Resource. The superior matching of q_m values as obtained via Langmuir and DKR models with the experimentally observed values (q_m (Exp)), along with the $\langle r^2 \rangle$ values close to unity, strongly suggests the validity of these isotherm models. Hence, in the present investigation, the equilibrium adsorption of MB on the surface of HTNF magnetic nanocomposites follows both Langmuir and DKR models which is in good agreement with the earlier reports by Narayani et al. 2013b and Harsha et al. 2015.

(Note: for the calculation of separation factor (R_L), adsorption energy (E), and change in Gibb's free energy (ΔG^0); see the section-O of Online Resource). The R_L values for MB

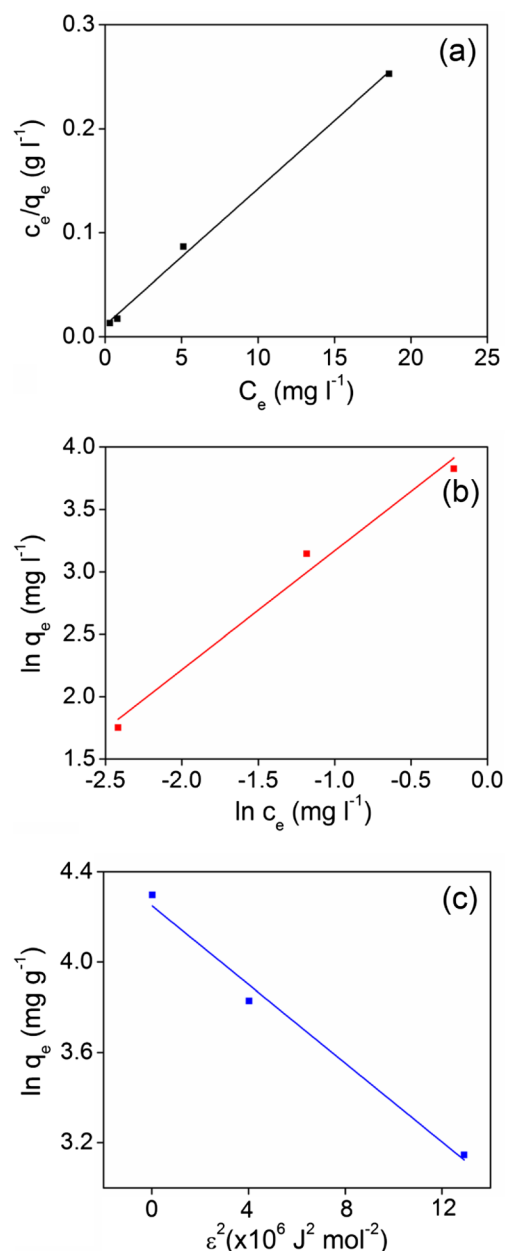


Fig. 8 Typical Langmuir (a), Freundlich (b), and DKR (c) plots as obtained for HTNF-5 sample

adsorption on the surface of both pure HTN and HTNF magnetic nanocomposites lie in between 0.002 and 0.55 (see the Table S4 of Online Resource), which indicate that the adsorption process is favorable. According to Shen et al. (2010), when the E value is in between 8 and 16 kJ mol⁻¹, the adsorption is due to ion-exchange reactions, while that less than 8 kJ mol⁻¹ supports the electrostatic attraction mechanism. Both the negative values of ΔG^0 and E values less than 8 kJ mol⁻¹ (see the Table S4 of Online Resource) strongly suggest the spontaneous monolayer MB adsorption on the surface of HTNF samples via electrostatic attraction mechanism.

Magnetic separation, regeneration, and reuse of HTNF magnetic nanocomposite

The magnetic hysteresis loops obtained for HTNF samples at room temperature are displayed in Fig. 9. The S-like hysteresis loops, very low values of remanence field and coercivity, indicate the superparamagnetic nature of nanocomposites. The magnetic nanoparticles of γ -Fe₂O₃ possess relatively higher saturation magnetization value of 71 emu g⁻¹. It is noted that the magnetization of HTNF nanocomposites is gradually decreased from HTNF-1 to HTNF-7 sample due to decrease in the weight fraction of γ -Fe₂O₃ nanoparticles. The saturation magnetization values are noted to be 62, 52, 36, and 34 emu g⁻¹ for HTNF-1, HTNF-3, HTNF-5, and HTNF-7 samples, respectively. Appreciable magnetization values enable their fast separation from the treated aqueous solution in less than a minute. The digital photograph of separation process as demonstrated for HTNF-5 magnetic nanocomposite particles, after the surface adsorption of MB dye in an aqueous solution, is presented as an inset in Fig. 9.

As demonstrated by Konicki et al. (2013), the regeneration of adsorption sites is generally achieved by desorbing the adsorbent molecules using organic solvents such as acetone, ethanol, acrylonitrile, and ethyl acetate. In the case of acidic and basic dyes, this is accomplished by Zhang et al. (2013) by adjusting the solution-pH using NaOH and HCl solutions, respectively. However, these techniques merely transfer the organics from the catalyst surface to the desorption medium, thus creating a secondary pollution. The other most commonly employed techniques for the regeneration of adsorbents are thermal decomposition, photocatalytic, and chemical oxidation which are energy-sensitive techniques (Teixeira et al. 2014; Haitham et al. 2014; Lin and Wang 2003). In this respect, the recycling of titanate nanotubes via oxidative catalytic process

involving the activation of H₂O₂, as recently demonstrated by us (Babu et al. 2014) and others (Lorencon et al. 2014; Zhou et al. 2015b), is highly noteworthy since the surface-adsorbed organics are completely decomposed in an aqueous solution in the dark. The recent review by Schneider et al. (2014) suggests that the dynamics of radical ion generation and their role in the dye decomposition process have been thoroughly investigated for the photocatalysis mechanism. Nevertheless, such study for the non-radiation driven H₂O₂ activation using the semiconductor oxide nanostructures, such as the titanate nanotubes, is very limited (Lorencon et al. 2014; Zhou et al. 2015b) Hence, the recyclability of HTNF magnetic nanocomposite is demonstrated here through the catalytic decomposition of surface-adsorbed MB molecules via non-radiation driven H₂O₂ activation.

The obtained variation in the amount of MB dye adsorbed on the surface of HTNF-5 sample for six successive cycles of dye adsorption, conducted without and with the involvement of regeneration treatment, is shown as a bar diagram in Fig. 10. It is clearly observed that without the regeneration treatment, the MB adsorption on the surface of HTNF-5 sample decreases almost by ~89%. Comparison, however, shows that only a marginal decrease of 1.5% is observed with the involvement of regeneration treatment conducted in the H₂O₂ solution. This strongly suggests that without the regeneration treatment, more number of potential sites available for MB adsorption on the surface of HTNF-5 sample is consumed resulting in a progressive decrease in the amount of MB dye adsorbed after each cycle of dye adsorption. The regeneration treatment conducted in H₂O₂ solution, however, decomposes the dye already adsorbed in the previous cycle resulting in the restoration of all potential sites available for MB adsorption on the catalyst surface. As a result, the amount of MB dye adsorbed remains very high for each successive cycle of dye adsorption.

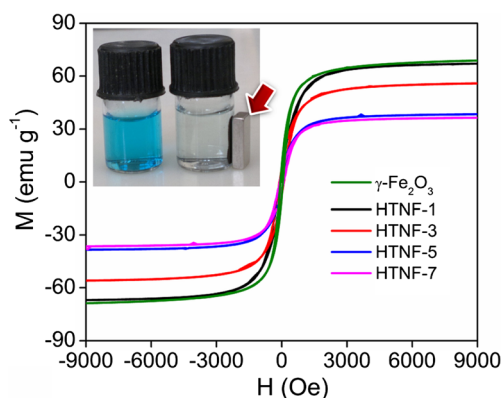


Fig. 9 Magnetization curves as obtained for pure γ -Fe₂O₃ nanoparticles and HTNF samples. The inset in upper-left corner shows the magnetic separation of HTNF-5 sample in an aqueous solution using an external bar magnet which is indicated by an arrow. *M*, intensity of magnetization; *H*, magnetizing field strength

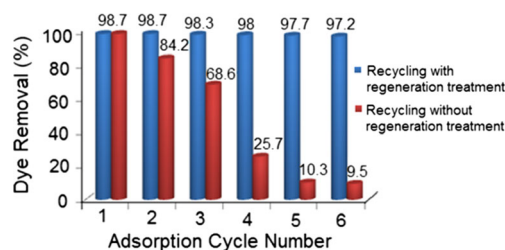
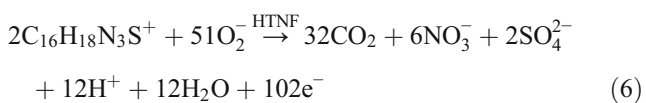
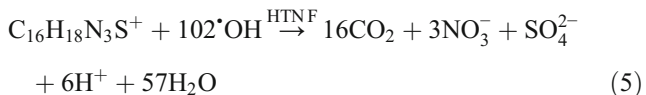


Fig. 10 Variation in the normalized concentration of MB dye adsorbed after 1 h of contact time as a function of dye adsorption cycle number as obtained for HTNF-5 sample without and with the involvement of regeneration treatment conducted after each dye adsorption cycle. For MB adsorption, the test conditions are: initial MB concentration = 30 μ M, catalyst concentration = 0.4 g l⁻¹, and initial solution-pH = 10. For the regeneration treatment, the test conditions are: initial H₂O₂ concentration = 15 wt% (4.5 M), MB-loaded catalyst concentration = 0.4 g l⁻¹, and contact time = 3 h

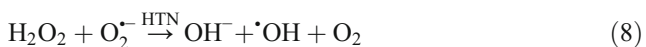
Mechanism of MB degradation on the surface of HTNF magnetic nanocomposite via non-radiation driven H₂O₂ activation

The HTNF-5 magnetic nanocomposite essentially contains 31 wt% of HTN and balance γ -Fe₂O₃ nanoparticles as the major constituents. According to Wang et al. (2013), the degradation of an organic synthetic dye such as MB via Fenton-like reactions takes place via generation and attack of ROS such as O₂⁻ and ·OH. As suggested by Houas et al. (2001), MB dye decomposition may occur as

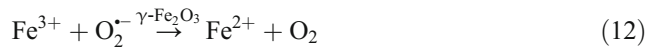


(Note: the generated electrons in the Eq. 6 may be picked by dissolved O₂). Hence, in order to confirm the proposed mechanism of MB decomposition on the surface of HTNF-5 magnetic nanocomposite via non-radiation driven activation of H₂O₂ and also to elucidate the precise role of individual catalyst components, O₂⁻ and ·OH were trapped using two different radical trapping agents. The qualitative variation in the concentration of ·OH produced after 10 min of contact time for different catalysts is presented and compared in Fig. 11a. It is noted that both pure HTN and pure γ -Fe₂O₃ nanoparticles produce relatively lower concentration of ·OH. Moreover, the concentration of ·OH produced by pure γ -Fe₂O₃ nanoparticles is relatively higher than that produced by pure HTN. However, the concentration of ·OH generated by HTNF-5 magnetic nanocomposite is much higher than that produced by individual components and their cumulative effect which strongly suggests a positive synergy effect in between them.

It has been proposed that the activation of H₂O₂ in the presence of pure HTN results in the generation of ·OH via following sequence of chemical reactions which includes the well-known Haber–Weiss reaction (Babu et al. 2014; Costa et al. 2006).



Moreover, pure γ -Fe₂O₃ nanoparticles are also responsible for the generation ·OH via following Fenton-like reactions (Wang et al. 2012).



The positive synergy effect between HTN and γ -Fe₂O₃ nanoparticles in the generation of ·OH can be explained based on the chemical reactions presented in the Eqs. 7–12. It appears that large amount of O₂⁻ are produced by HTN alone (Eqs. 7 and 9) which may drive the chemical reaction presented in the Eq. 12 in the forward direction when both HTN and γ -Fe₂O₃ nanoparticles are simultaneously present in H₂O₂ solution in the form of HTNF-5 magnetic nanocomposite. As a consequence, for HTNF-5 magnetic nanocomposite, the concentration of Fe²⁺ ions is relatively higher than that of pure γ -Fe₂O₃ nanoparticles which results in the generation of relatively higher concentration of ·OH via chemical reaction presented in the Eqs. 8 and 11 as noted in Fig. 11a.

It, hence, appears that during the operation of above mechanism involving the non-radiation driven activation of H₂O₂ using magnetic HTNF-5 sample, the concentration of O₂⁻ produced by latter must be lower than that of pure HTN. In order to confirm this hypothesis, the qualitative variation in the concentration of O₂⁻ produced after 10 min of contact time is presented and compared in Fig. 11b for different catalysts. It is clear that both pure HTN and pure γ -Fe₂O₃ nanoparticles produce O₂⁻. Using the electron paramagnetic resonance (EPR) and X-ray photoelectron spectroscopy (XPS) spectroscopy analyses, Lorencon et al. (2014) and Zhou et al. (2015b) confirmed that O₂⁻ are generated via non-radiation driven activation of H₂O₂ by pure HTN and are responsible for the decomposition of MB and Rhodamine B dyes. In Fig. 11b, the concentration of O₂⁻ produced by pure HTN is observed to be relatively higher than that produced by pure γ -Fe₂O₃ nanoparticles. However, the concentration of O₂⁻ generated by HTNF-5 magnetic nanocomposite is lower than that produced by individual components and much lower than their cumulative effect. Thus, a negative synergy effect is undoubtedly observed in between HTN and γ -Fe₂O₃ nanoparticles in the generation of O₂⁻ which strongly supports the mechanism proposed above for the generation of ·OH via non-radiation driven activation of H₂O₂ using HTNF-5 magnetic nanocomposite. Hence, in the case of HTNF-5 magnetic nanocomposite, the generated O₂⁻ are rapidly consumed and converted to ·OH as a consequence of synergy effect of two components. The net result is that the concentration of ·OH produced by non-radiation driven activation of H₂O₂ using HTNF-5 sample is very high, while that of O₂⁻ is very low (Fig. 11). It is noted that since the activation of H₂O₂ is achieved in the dark condition, the difference in the band gap energy (*E_{bg}*) values of pure HTN and γ -Fe₂O₃ nanoparticles does not have any significant contribution in the formation of

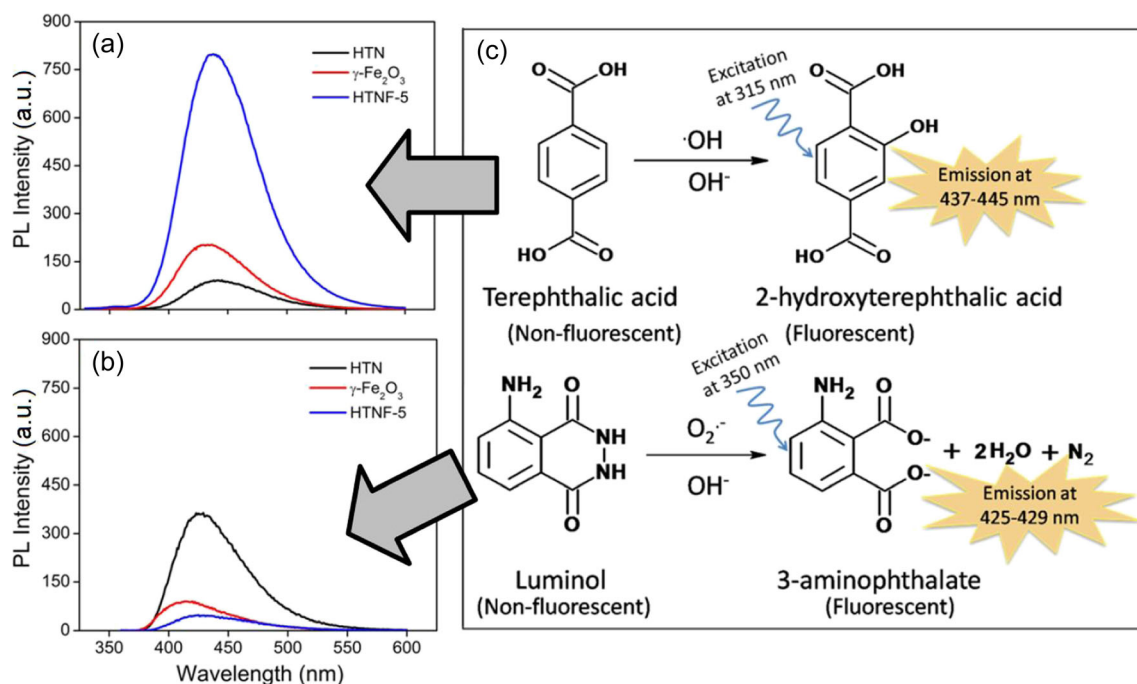


Fig. 11 PL intensities in the visible range associated with 2-hydroxyterephthalic acid (a) and 3-aminophthalate (b) formed as a result of radical trapping (c), after the contact time of 10 min, as observed for different catalysts at the excitation wavelengths of 315

(a) and 350 nm (b). PL intensities observed in a and b are proportional to the concentration of $\cdot\text{OH}$ and $\text{O}_2^{\cdot-}$ produced as a result of activation of H_2O_2 using different catalysts. Initial H_2O_2 concentration = 15 wt% (4.5 M)

$\text{O}_2^{\cdot-}$ and $\cdot\text{OH}$ (see Fig. S11 and related discussion in the Online Resource).

Based on the above results, the degradation of MB dye on the surface of HTNF-5 sample (that is, the regeneration treatment) is attributed to the predominance of chemical reaction presented in the Eq. 5 over that presented in the Eq. 6. This is in contrast to pure HTN for which the degradation of MB dye on their surfaces appears to be predominantly via chemical reaction presented in the Eq. 6 than that presented in the Eq. 5. It is further noted that, in the present investigation, the non-radiation driven activation of H_2O_2 is achieved using the combination of magnetic γ -Fe₂O₃ nanoparticles and non-magnetic nanotubes of $\text{H}_2\text{Ti}_3\text{O}_7$ which is in contrast to the activation of H_2O_2 normally reported under the UV-radiation exposure for the semiconductor oxides (such as TiO_2) based photocatalysis mechanism (Wong and Chu 2003). Thus, for the first time, the precise role of ROS and the underlying dye decomposition mechanism are elucidated here using the different radical trapping agents via PL studies which clearly reveal the synergy effect of constituents of HTNF magnetic nanocomposite.

Overall, the various steps, such as the surface adsorption of an organic dye with the effective magnetic separation of nanocomposite from the treated solution followed by dye degradation in the dark via ROS attack achieved through the non-radiation driven H_2O_2 activation, when sequentially combined

together provide a systematic approach (see the Scheme S2 of Online Resource) for the removal of MB dye from the aqueous solution, which may be utilized in the near-future for the removal of other types synthetic dyes.

Conclusions

Mesoporous magnetic nanocomposite consisting of $\text{H}_2\text{Ti}_3\text{O}_7$ nanosheets/nanotubes and γ -Fe₂O₃ nanoparticles is successfully synthesized via hydrothermal treatment of core-shell γ -Fe₂O₃/SiO₂/TiO₂ magnetic photocatalyst having different amounts of TiO₂ in the shell. $\text{H}_2\text{Ti}_3\text{O}_7$ phase having different shapes such as nanosheets, nanotubes, and mixed morphologies is evolved depending on the amount of TiO₂ in the shell of precursor. A model has been proposed to explain such variations in the observed morphologies of $\text{H}_2\text{Ti}_3\text{O}_7$ in the HTNF magnetic nanocomposite as a function of increasing amount of TiO₂. The variation in MB adsorption capacity of HTNF magnetic nanocomposite is well correlated with that of specific surface area and pore volume as a function of amount of γ -Fe₂O₃ nanoparticles. The magnetic HTNF-5 sample containing 31 wt% HTN exhibits the highest MB adsorption capacity (74 mg g⁻¹) and is ascribed to its higher specific surface area and pore volume. The equilibrium adsorption of cationic MB on the surface of HTNF-5 magnetic nanocomposite

follows the pseudo-second-order kinetics and Langmuir and DKR isotherm models. The recyclability (that is, regeneration and reuse) of HTNF-5 sample in the dye removal application is achieved via magnetic separation and decomposition of previously adsorbed MB on the catalyst surface via non-radiation driven H_2O_2 activation involving synergy effect between the constituents of HTNF-5 magnetic nanocomposite.

Acknowledgements The authors thank CSIR, India for funding the research projects no. MLP0012, OLP216339, P81113 and providing the Senior Research Fellowships (SRFs) to HN and MJ. The authors also thank Mr. Kiran, Mr. Firozkhan, Mr. A. Peermohamed, and Mr. Ajeesh (CSIR-NIIST, India) for conducting the TEM, XRD, BET, and PPMS analyses, respectively.

References

- Abramson S, Srithammavanh L, Siaugue JM, Horner O, Xu X, Cabuil V (2009) Nanometric core-shell-shell $\gamma\text{-Fe}_2\text{O}_3/\text{SiO}_2/\text{TiO}_2$ particles. *J Nanopart Res* 11:459–465
- Babu KB, Warriar KG, Shukla S (2014) Decolorization of aqueous solution containing organic synthetic-dye via dark-catalysis process using hydrothermally synthesized semiconductor-oxides nanotubes. *Adv Sci Eng Med* 6:173–183
- Bavykin DV, Friedrich JM, Lapkin AA, Walsh FC (2006) Stability of aqueous suspensions of titanate nanotubes. *Chem Mater* 18:1124–1129
- Bavykin DV, Redmond KE, Nias BP, Kulak AN, Walsh FC (2010) The effect of ionic charge on the adsorption of organic dyes onto titanate nanotubes. *Aust J Chem* 63:270–275
- Beydoun D, Amal R, Low G, McEvoy S (2002) Occurrence and prevention of photodissolution at the phase junction of magnetite and titanium dioxide. *J Mol Catal A* 180:193–200
- Costa RC, Lelis M, Oliveira L, Fabris J, Ardisson JD, Rios R, Silva C, Lago R (2006) Novel active heterogeneous Fenton system based on $\text{Fe}_{3-x}\text{M}_x\text{O}_4$ (Fe, Co, Mn, Ni): the role of M^{2+} species on the reactivity towards H_2O_2 reactions. *J Hazard Mater* 129:171–178
- Freundlich H (1906) Over the adsorption in solution. *J Phys Chem* 57:385–470
- Gracia-Espino E, Lopez-Urias F, Terrones H, Terrones M (2012) Novel nanocarbons for adsorption. In: Tascon JMD (ed) Novel carbon adsorbents. Elsevier, Amsterdam, pp 3–34Chapter 1
- Gunathilake C, Kadanapitiye MS, Dudarko O, Huang SD, Jaroniec M (2015) Adsorption of lead ions from aqueous phase on mesoporous silica with P-containing pendant groups. *ACS Appl Mater Interfaces* 7:23144–23152
- Gupta VK, Suhas (2009) Application of low-cost adsorbents for dye removal - a review. *J Environ Manag* 90:2313–2342
- Haitham K, Razak S, Nawi M (2014) Kinetics and isotherm studies of methyl orange adsorption by a highly recyclable immobilized polyaniline on a glass plate. *Arab J Chem*. doi:10.1016/j.arabj.2014.10.010
- Hareesh P, Babitha KB, Shukla S (2012) Processing fly ash stabilized hydrogen titanate nano-sheets for industrial dye-removal application. *J Hazard Mater* 229-230:177–182
- Harsha N, Krishna KVS, Renuka NK, Shukla S (2015) Facile synthesis of $\gamma\text{-Fe}_2\text{O}_3$ nanoparticles integrated $\text{H}_2\text{Ti}_3\text{O}_7$ nanotubes structure as a magnetically recyclable dye-removal catalyst. *RSC Adv* 5:30354–30362
- Ho YS, McKay G (1998) Sorption of dye from aqueous solution by peat. *Chem Eng J* 70:115–124
- Houas A, Lachheb H, Ksibi M, Elaloui E, Guillard C, Herrmann JM (2001) Photocatalytic degradation pathway of methylene blue in water. *Appl Catal B* 31:145–157
- Ishibashi KI, Fujishima A, Watanabe T, Hashimoto K (2000) Detection of active oxidative species in TiO_2 photocatalysis using the fluorescence technique. *Electrochem Commun* 2:207–210
- Jose M, Haridas MP, Shukla S (2014) Predicting dye-adsorption capacity of hydrogen titanate nanotubes via one-step dye-removal method of novel chemically-activated catalytic process conducted in dark. *J Environ Chem Eng* 2:1980–1988
- Kitano M, Wada E, Nakajima K, Hayashi S, Miyazaki S, Kobayashi H, Hara M (2013) Protonated titanate nanotubes with Lewis and Bronsted acidity: relationship between nanotube structure and catalytic activity. *Chem Mater* 25:385–393
- Konicki W, Sibera D, Mijowska E, Lendzion-Bieluń Z, Narkiewicz U (2013) Equilibrium and kinetic studies on acid dye acid red 88 adsorption by magnetic ZnFe_2O_4 spinel ferrite nanoparticles. *J Colloid Interface Sci* 398:152–160
- Lagergren S (1898) About the theory of so-called adsorption of soluble substances. *Kung Sven Vetén Hand* 24:1–39
- Lakouraj MM, Norouzian RS, Balo S (2015) Preparation and cationic dye adsorption of novel Fe_3O_4 supermagnetic/thiacalix[4]arene tetrasulfonate self-doped/polyaniline nanocomposite: kinetics, isotherms, and thermodynamic study. *J Chem Eng Data* 60:2262–2272
- Langmuir I (1916) The constitution and fundamental properties of solids and liquids part I. solids. *J Am Chem Soc* 38:2221–2295
- Lee CK, Lin KS, Wu CF, Lyu MD, Lo CC (2008) Effects of synthesis temperature on the microstructures and basic dyes adsorption of titanate nanotubes. *J Hazard Mater* 150:494–503
- Lee CK, Fen SK, Chao HP, Liu SS, Huang FC (2012) Effects of pore structure and surface chemical characteristics on the adsorption of organic vapors on titanate nanotubes. *Adsorption* 18:349–357
- Li W, Deng Y, Wu Z, Qian X, Yang J, Wang Y, Gu D, Zhang F, Tu B, Zhao D (2011) Hydrothermal etching assisted crystallization: a facile route to functional yolk-shell titanate microspheres with ultrathin nanosheets-assembled double shells. *J Am Chem Soc* 133:15830–15833
- Lin SH, Wang CH (2003) Adsorption and catalytic oxidation of phenol in a new ozone reactor. *Environ Technol* 24:1031–1039
- Liu SQ (2012) Magnetic semiconductor nano-photocatalysts for the degradation of organic pollutants. *Environ Chem Lett* 10:209–216
- Lorencon E, Brandao FD, Krambrock K, Alves DCB, Silva JCC, Ferlauto AS, Lago RM (2014) Generation of reactive oxygen species in titanates nanotubes induced by hydrogen peroxide and their application in catalytic degradation of methylene blue dye. *J Mol Catal A* 394:316–323
- Lu H, Zhao J, Li L, Zheng J, Zhang L, Gong L, Wang Z, Zhu Z (2011) A systematic study on evolution mechanism of titanate nanostructures in the hydrothermal process. *Chem Phys Lett* 508:258–264
- Narayani H, Arayapurath H, Shukla S (2013a) Significance of silica interlayer in magnetic photocatalyst having $\gamma\text{-Fe}_2\text{O}_3$ as a magnetic ceramic core. *Sci Adv Mater* 5:1060–1073
- Narayani H, Kunniveetil SP, Shukla S (2013b) Effect of solution-pH on methylene blue dye adsorption on hydrogen titanate nanotubes processed via hydrothermal method. *Adv Sci Eng Med* 5:63–72
- Nosaka Y, Yamashita Y, Fukuyama H (1997) Application of chemiluminescent probe to monitoring superoxide radicals and hydrogen peroxide in TiO_2 photocatalysis. *J Phys Chem B* 101:5822–5827
- Papa AL, Maurizi L, Vandroux D, Walker P, Millot N (2011) Synthesis of titanate nanotubes directly coated with USPIO in hydrothermal conditions: a new detectable nanocarrier. *J Phys Chem C* 115:19012–19017
- Schneider J, Matsuoka M, Takeuchi M, Zhang J, Horiuchi Y, Anpo M, Bahnemann DW (2014) Understanding TiO_2 photocatalysis: mechanisms and materials. *Chem Rev* 114:9919–9986

- Shen S, Pan T, Liu X, Yuan L, Wang J, Zhang Y, Guo Z (2010) Adsorption of Rh(III) complexes from chloride solutions obtained by leaching chlorinated spent automotive catalysts on ion-exchange resin. *J Hazard Mater* 179:104–112
- Shukla S, Oturan MA (2015) Dye removal using electrochemistry and semiconductor oxide nanotubes. *Environ Chem Lett* 13:157–172
- Shukla SV, Warriar, KGK, Babu BK (2014) Publication Date: 20-February, World Intellectual Property Organization (WIPO) Publication Number WO/2014/027364
- Sivashankar R, Sathya A, Vasantharaj K, Sivasubramanian V (2014) Magnetic composite an environmental super adsorbent for dye sequestration—a review. *Environ Nanotechnol Monit Manage* 1:36–49
- Tan I, Ahmad AL, Hameed B (2008) Adsorption of basic dye on high-surface-area activated carbon prepared from coconut husk: equilibrium, kinetic and thermodynamic studies. *J Hazard Mater* 154:337–346
- Teixeira TPF, Aquino SF, Pereira SI, Dias A (2014) Use of calcined layered double hydroxides for the removal of color and organic matter from textile effluents: kinetic, equilibrium and recycling studies. *J Chem Eng* 31:19–26
- Thazhe L, Shereef A, Shukla S, Reshmi CP, Varma MR, Suresh KG, Patil K, Warriar KG (2010) Magnetic dye-adsorbent catalyst: processing, characterization, and application. *J Am Ceram Soc* 93:3642–3650
- Wang C, Yin L, Zhang L, Kang L, Wang X, Gao R (2009) Magnetic (γ - Fe_2O_3 @ SiO_2) N@ TiO_2 functional hybrid nanoparticles with activated photocatalytic ability. *J Phys Chem* 113:4008–4011
- Wang C, Liu H, Sun Z (2012) Heterogeneous photo-Fenton reaction catalyzed by nanosized iron oxides for water treatment. *Int J Photoenergy*. doi:10.1155/2012/801694
- Wang Q, Tian S, Ning P (2013) Degradation mechanism of methylene blue in a heterogeneous Fenton-like reaction catalyzed by ferrocene. *Eng Chem Res* 53:643–649
- Wong C, Chu W (2003) The hydrogen peroxide-assisted photocatalytic degradation ofalachlor in TiO_2 suspensions. *Environ Sci Technol* 37:2310–2316
- Wu D, Liu J, Zhao X, Li A, Chen Y, Ming N (2006) Sequence of events for the formation of titanate nanotubes, nanofibers, nanowires, and nanobelts. *Chem Mater* 18:547–553
- Yu X, Liu S, Yu J (2011) Superparamagnetic γ - Fe_2O_3 @ SiO_2 @ TiO_2 composite microspheres with superior photocatalytic properties. *Appl Catal B* 104:12–20
- Zhang YR, Wang SQ, Shen SL, Zhao BX (2013) A novel water treatment magnetic nanomaterial for removal of anionic and cationic dyes under severe condition. *Chem Eng J* 233:258–264
- Zhou L, Xu M, Wei G, Li L, Chubik M, Chubik MP, Gromov AA, Han W (2015a) Fe_3O_4 @titanate nanocomposites: novel reclaimable adsorbents for removing radioactive ions from wastewater. *J Mater Sci Mater Electron* 26:2742–2747
- Zhou C, Luo J, Chen Q, Jiang Y, Dong X, Cui F (2015b) Titanate nanosheets as highly efficient non-light-driven catalysts for degradation of organic dyes. *Chem Commun* 51:10847–10849